

# Discharge modeling in EAST using bidirectional LSTM

Chenguang Wan<sup>1,2,\*</sup>, Zhi Yu<sup>1</sup>, Alessandro Pau<sup>3</sup>, Xiaojuan Liu<sup>1</sup> and  
Jiangang Li<sup>1,2,\*</sup>

1. Institute of Plasma Physics, Hefei Institutes of Physical Science, Chinese Academy of Sciences, Hefei 230031, China
2. University of Science and Technology of China, Hefei, 230026, China
3. École Polytechnique Fédérale de Lausanne (EPFL), Swiss Plasma Center (SPC), CH-1015 Lausanne, Switzerland

E-mail: [chenguang.wan@ipp.ac.cn](mailto:chenguang.wan@ipp.ac.cn) and [j\\_li@ipp.ac.cn](mailto:j_li@ipp.ac.cn)

**Abstract.** An improved discharge model based on a bidirectional neural network was developed. The bidirectional long short-term memory (LSTM) model was used, and it was trained by the experimental data from the Experimental Advanced Superconducting Tokamak (EAST) campaign 2010-2020 discharges. Compared to our previous works (Chenguang Wan et al 2021 *Nucl. Fusion* **61** 066015), the present work integrates the reconstruction of the discharge evolution process with additional key diagnostic signals, including the electron density  $n_e$ , store energy  $W_{mhd}$ , loop voltage  $V_{loop}$ , actual plasma current  $I_p$ , normalized beta  $\beta_n$ , toroidal beta  $\beta_t$ , beta poloidal  $\beta_p$ , elongation at plasma boundary  $\kappa$ , internal inductance  $l_i$ ,  $q$  at magnetic axis  $q_0$ , and  $q$  at 95% flux surface  $q_{95}$ . The accuracy in the reconstruction of density  $n_e$  and loop voltage  $V_{loop}$  is improved by respectively  $\sim 1\%$  and  $\sim 5\%$  compared to our previous work. The average similarity of all the selected key diagnostic signals between modeling results and the experimental data are greater than 90%, except for the  $V_{loop}$  and  $q_0$ . Before a tokamak experiment, the values of actuators signals are set in the discharge proposal stage, the model allowing to check the consistency of expected diagnostic signals. The model can give the estimated values of the diagnostic signals to check the reasonableness of the tokamak experimental proposal.

*Keywords:* discharge modeling, machine learning, bidirectional LSTM Submitted to: *Nucl. Fusion*

## 1. Introduction

The entire modeling of a discharge in a tokamak is a complicated, critical, and urgent problem to be solved. It is used to check the consistency of the modeled diagnostic signals, assist in experimental data analysis, validate theoretical models, control technology R&D, and provide references for the design of an experiment [1]. In the framework of conventional discharge modeling, from a physics point of view, the primary method is "Integrated Modeling" [2] derived from first principles. "Integrated Modeling" involves lots of different physical processes in tokamak. Integrated modeling accuracy depends on the completeness and rationality of the tokamak's physics derivations at the base of the model itself. Due to the nonlinear, multi-scale, multi-physics characteristics of the tokamak, high-fidelity and faster simulation and plasma control of the whole tokamak discharge is still a great scientific challenge [3].

A neural network method is an alternative approach for tokamak discharge modeling without integrating the complex physical model. The method have been employed in magnetic fusion research to solve a variety of problems, including disruption prediction [4–10], simulation acceleration [11–13], plasma tomography [14], radiated power estimation [15], identification of instabilities [16], estimation of neutral beam effects [17], classifying confinement regimes [18], determination of scaling laws [19, 20], filament detection on MAST-U [21], electron temperature profile estimation via SXR with Thomson scattering [22], coil current prediction with the heat load pattern in W7-X [23], equilibrium reconstruction [22, 24–28], and equilibrium solver [29], control plasma [30–35], physic-informed machine learning [36]. Additionally, our previous work [1] used a neural-network-based method for discharge modeling. In this work, only the backward (past) observation information was used without considering the forward (future) information. Offline discharge modeling differs from disruption prediction and the model can benefit of a wider context, where backward and forward information are in principle equally important to describe the dynamic of the system. Another limitation of the previous work is the modeling of a restricted set of signals (electron density  $n_e$ , stored energy  $W_{mhd}$ , and loop voltage  $V_{loop}$ ), which is still not enough for tokamak discharge modeling. Moreover, the model requires the integration of a physical model code to estimate the actual  $I_p$  as input signal. So in this paper, a new machine learning architecture was designed to consider wider contextual information, modeling eleven key signals of tokamak discharge, and values of all the input signals can be directly available or given by the machine learning model without integrating physical codes.

In the present work, we trained a bidirectional LSTM model using large-scale data from EAST tokamak [37–39] during 2010–2020 campaigns. Bidirectional LSTM [40–42] connects two hidden layers with the information propagating in opposite directions to the same output. The output layer can simultaneously get information from backward and forward states with these designations. With the 85 actuator signals (introduce further in table 1) as input, the model is able to reproduce the whole tokamak discharge time evolution of eleven key diagnostic signals, that are the electron density  $n_e$ , store energy  $W_{mhd}$ , loop voltage  $V_{loop}$ , actual plasma current  $I_p$ , normalized beta  $\beta_n$ , toroidal beta  $\beta_t$ , beta poloidal  $\beta_p$ , elongation at plasma boundary  $\kappa$ , internal inductance  $l_i$ , q at magnetic axis  $q_0$ , and q at 95% flux surface  $q_{95}$ .

This paper is organized as follows. First, section 2 details the deep learning model architecture. Then, section 3 describes the data preprocessing and selection criteria. The detailed model training process can be found in section 4. Next, section 5 presents the experimental evaluation, and a comparison with the previous work is given in section 5. Finally, the results are discussed, and a brief conclusion is made in section 6.

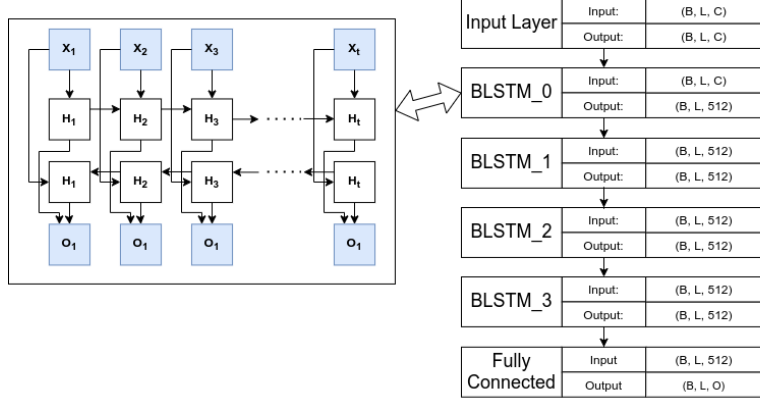


**Figure 1.** The architecture of bidirectional LSTM. The subfigure on the left represents a bidirectional LSTM cell. Here, B, L, C are batch size, the longest sequence length of batch, feature size, and the number of output signal channels.

## 2. Model

This work aims to overcome the limitation of previous discharge modeling with machine learning. In the previous work [1], an encoder-decoder architecture was adapted, only the information before the current calculation time point (past information) was used without introducing the wider contextual information. In this work, an improved bidirectional Recurrent Neural Network (RNN) [40–42] was developed, and contextual information was taken into account. In this paper, our deep learning architecture stacked four bidirectional LSTM cells.

Theoretically, the bidirectional LSTM network concentrates on minimizing the objective function for both time directions simultaneously. There is no need to search for an “optimal delay” to minimize the objective function in a given data/network structure combination because all future and past information around the currently evaluated time point is theoretically available and does not depend on an individually defined delay parameter. We regard the tokamak discharge evolution as a sequence-to-sequence process, as in the language translation task, we relax the causality constraint to access larger contextual information. It has been shown in several works [REFERENCES] that a bidirectional LSTM is often able to model more efficiently. Bidirectional long-term dependencies between time steps of time series or sequence data, and this is particularly useful for regression tasks. The network, having access to the complete time series at each time step, will be more robust to the noise in the reconstruction of the tokamak discharge improving the similarity of the reconstructed parameters. In practice, the present BiLSTM is more efficient than previous work. Since it can be used without adaptive resampling and integrating the actual plasma current  $I_p$ .

Figure 1 shows the deep learning model architecture stacked four bidirectional LSTMs. For any time step  $t$ , we define the mini-batch input as  $\mathbf{X}_t \in \mathbb{R}^{n \times d}$  (number of examples:  $n$ , number of input features in each example:  $d$ ). In per layer bidirectional LSTM, we assume that the forward and backward hidden states for this time step are  $\overrightarrow{\mathbf{H}}_t \in \mathbb{R}^{n \times h}$  and  $\overleftarrow{\mathbf{H}}_t \in \mathbb{R}^{n \times h}$ , respectively, where  $h$  is the number of hidden units. The forward and backward hidden state updates are as follows:

$$\overrightarrow{\mathbf{i}}_t = \sigma \left( \mathbf{W}_{ii}^{(f)} \mathbf{X}_t + \mathbf{b}_{ii}^{(f)} + \mathbf{W}_{hi}^{(f)} \overrightarrow{\mathbf{H}}_{t-1} + \mathbf{b}_{hi}^{(f)} \right)$$

$$\begin{aligned}
\overrightarrow{\mathbf{f}}_t &= \sigma \left( \mathbf{W}_{if}^{(f)} \mathbf{X}_t + \mathbf{b}_{if}^{(f)} + \mathbf{W}_{hf}^{(f)} \overrightarrow{\mathbf{H}}_{t-1} + \mathbf{b}_{hf}^{(f)} \right) \\
\overrightarrow{\mathbf{g}}_t &= \tanh \left( \mathbf{W}_{ig}^{(f)} \mathbf{X}_t + \mathbf{b}_{ig}^{(f)} + \mathbf{W}_{hg}^{(f)} \overrightarrow{\mathbf{H}}_{t-1} + \mathbf{b}_{hg}^{(f)} \right) \\
\overrightarrow{\mathbf{o}}_t &= \sigma \left( \mathbf{W}_{io}^{(f)} \mathbf{X}_t + \mathbf{b}_{io}^{(f)} + \mathbf{W}_{ho}^{(f)} \overrightarrow{\mathbf{H}}_{t-1} + \mathbf{b}_{ho}^{(f)} \right) \\
\overrightarrow{\mathbf{c}}_t &= \overrightarrow{\mathbf{f}}_t \odot \overrightarrow{\mathbf{c}}_{t-1} + \overrightarrow{\mathbf{i}}_t \odot \overrightarrow{\mathbf{g}}_t \\
\overrightarrow{\mathbf{H}}_t &= \overrightarrow{\mathbf{o}}_t \odot \tanh(\overrightarrow{\mathbf{c}}_t)
\end{aligned} \tag{1}$$

$$\begin{aligned}
\overleftarrow{\mathbf{i}}_t &= \sigma \left( \mathbf{W}_{ii}^{(f)} \mathbf{X}_t + \mathbf{b}_{ii}^{(f)} + \mathbf{W}_{hi}^{(f)} \overleftarrow{\mathbf{H}}_{t+1} + \mathbf{b}_{hi}^{(f)} \right) \\
\overleftarrow{\mathbf{f}}_t &= \sigma \left( \mathbf{W}_{if}^{(f)} \mathbf{X}_t + \mathbf{b}_{if}^{(f)} + \mathbf{W}_{hf}^{(f)} \overleftarrow{\mathbf{H}}_{t+1} + \mathbf{b}_{hf}^{(f)} \right) \\
\overleftarrow{\mathbf{g}}_t &= \tanh \left( \mathbf{W}_{ig}^{(f)} \mathbf{X}_t + \mathbf{b}_{ig}^{(f)} + \mathbf{W}_{hg}^{(f)} \overleftarrow{\mathbf{H}}_{t+1} + \mathbf{b}_{hg}^{(f)} \right) \\
\overleftarrow{\mathbf{o}}_t &= \sigma \left( \mathbf{W}_{io}^{(f)} \mathbf{X}_t + \mathbf{b}_{io}^{(f)} + \mathbf{W}_{ho}^{(f)} \overleftarrow{\mathbf{H}}_{t+1} + \mathbf{b}_{ho}^{(f)} \right) \\
\overleftarrow{\mathbf{c}}_t &= \overleftarrow{\mathbf{f}}_t \odot \overleftarrow{\mathbf{c}}_{t+1} + \overleftarrow{\mathbf{i}}_t \odot \overleftarrow{\mathbf{g}}_t \\
\overleftarrow{\mathbf{H}}_t &= \overleftarrow{\mathbf{o}}_t \odot \tanh(\overleftarrow{\mathbf{c}}_t)
\end{aligned} \tag{2}$$

where the  $\overrightarrow{\mathbf{H}}_t$ ,  $\overleftarrow{\mathbf{H}}_t$  are the forward and backward hidden states at time  $t$ ,  $\overrightarrow{\mathbf{c}}_t$ ,  $\overleftarrow{\mathbf{c}}_t$  are the forward and backward cell states at time  $t$ ,  $\overrightarrow{\mathbf{i}}_t$ ,  $\overleftarrow{\mathbf{i}}_t$ ,  $\overrightarrow{\mathbf{f}}_t$ ,  $\overleftarrow{\mathbf{f}}_t$ ,  $\overrightarrow{\mathbf{g}}_t$ ,  $\overleftarrow{\mathbf{g}}_t$ ,  $\overrightarrow{\mathbf{o}}_t$ ,  $\overleftarrow{\mathbf{o}}_t$  are the forward and backward output of input, forget, and output gates, respectively.  $\sigma$  is the sigmoid function, and  $\odot$  is the Hadamard product.

Next, we concatenate the forward and backward hidden states  $\overrightarrow{\mathbf{H}}_t$  and  $\overleftarrow{\mathbf{H}}_t$  to obtain the hidden state  $\mathbf{H}_t \in \mathbb{R}^{n \times 2h}$  to be fed into the next layer.

Then again, the same calculation as in equation 1,2. When we consider dropout, the hidden state  $\mathbf{H}_t \in \mathbb{R}^{n \times 2h}$  will be randomly masked as zeros with a ratio  $\delta$  (in this paper, the dropout rate is  $\delta = 0.1$ ) at each step during *training* phase. The dropout can easily help prevent overfitting [43].

Last, the output layer computes the output  $\mathbf{O}_t \in \mathbb{R}^{n \times q}$  (number of outputs:  $q$ ):

$$\mathbf{O}_t = \text{activation}(\mathbf{H}_t \mathbf{W}_{hq} + \mathbf{b}_q). \tag{3}$$

Here, the weight matrix  $\mathbf{W}_{hq} \in \mathbb{R}^{2h \times q}$  and the bias  $\mathbf{b}_q \in \mathbb{R}^{1 \times q}$  are the model parameters of the output layer.

One of the key features of a bidirectional LSTM is that information from both ends of the sequence estimates the output. The architecture uses future (forward) and past (backward) information to predict the current. The final layer activation function is a linear functions, since we are dealing with a regression task and we don't want to constrain output parameters values.

### 3. Dataset

The whole EAST's data system stores more than 3000 raw channels data and thousands of processed physical analysis data [44], which record the entire process of the tokamak discharge. Similar to the authors' previous paper [1], all the data of the tokamak was divided into three categories: configuration parameters, actuators signals, and diagnostic signals. The discharge modeling can be essentially reduced to mapping actuators (input) signals to diagnostic (output) signals.

In the present work, the output signal includes all important 0-D EAST diagnostic signals routinely made available after a discharge. The input signals include all the signals that may affect the output. Table 1 contains detailed information about input and output signals. The input signal “Ref. Shape” should be noted. According to the tokamak magnetic control system diagram [45], the shape references affect the in-vessel Rogowski coil current (IC1). So when estimating IC1, the shape reference data is required. Some of the selected signals are processed signals with a clear physical meaning, and others are unprocessed raw acquisition signals. Since some signals of the actual EAST experimental diagnostic system are not processed, we directly selected the unprocessed raw acquisition signals. As long as the input signals contain information to determine the output, although they are not process signals with well defined physical meaning, it will not affect the modeling result.

Tokamak discharge evolution is a complex nonlinear process, and there is no simple way to determine the connection between the actuator signals and the diagnostic signals. For different diagnostic parameters, they are determined by different inputs. In the previous work [1], the three signals  $W_{mhd}$ ,  $n_e$  and  $V_{loop}$  can be directly determined by the input signals. Nevertheless, in the present work, the input signals can not simply and directly determine all the output signals. In our model training experiment,  $l_i$ ,  $\beta_n$  can not be accurately estimated by the input signals that do not include IC1. When the input signals include the actual IC1, all output signals of the present work can be estimated. Since IC1 values cannot be obtained through direct measurement, they have been indirectly estimated through a machine learning model.

## 4. Training

This section will introduce model training and data processing in detail. The training model can be divided into four steps as follows:

- (i) Obtaining and resampling the data of the 97 data channels (including input, feedback, and output signals as shown in table 1) from the EAST source database, then storing it in HDF5 <sup>‡</sup> file with each HDF5 file data properties (standard deviation  $\delta$ , mean  $\mu$ , etc.) stored in MongoDB.
- (ii) Standardizing the data with z-scores <sup>§</sup> (also known as standard scores).
- (iii) Using bucketing (explained further in section 4.3) batch training for the deep learning model to be reconstructed IC1.
- (iv) Integrating the estimated IC1 as input for the eleven key diagnostic signals (table 1 output signals) reconstruction model training.

### 4.1. Obtaining and resampling

The dataset is selected from EAST tokamak during 2010-2020 campaigns and the discharge shot number in the range #14866-88283 [37-39]. A total of 26230 normal shots were selected. The normal shot means that no disruption occurred during this discharge, the flat-top lasts more than two seconds, the key signals (i.e., magnetic field, and actual plasma current  $I_p$ ) are complete, at

<sup>‡</sup> Hierarchical Data Format (HDF) is a set of file formats (HDF4, HDF5) designed to store and organize large amounts of data.

<sup>§</sup> z-score is calculated by  $z = (x - \mu)/\sigma$  where  $\mu$  is the mean of the population.  $\sigma$  is the standard deviation of the population.

**Table 1.** The list of signals. The “raw signal” means the original electrical signal, and these could be converted to signals with physical meaning. The IC1 was estimated using a machine learning model and then fed to the diagnostic signals (output) reconstruction model as input.

Signals	Physics meanings	Unit	Number of Channels	Sampling rate	Meaning of Channels
Output Signals					
Act. $I_p$	Actual plasma current	A	1	1kHz	Actual plasma current
$n_e$	Electron density	$10^{19} m^{-3}$	1	1kHz	Electron density
$W_{mhd}$	Plasma stored energy	J	1	20Hz	Plasma stored energy
$V_{loop}$	Loop voltage	V	1	1kHz	Loop voltage
$\beta_n$	Normalized beta	dimensionless	1	15Hz	Normalized beta
$\beta_t$	Toroidal beta	dimensionless	1	15Hz	Toroidal beta
$\beta_p$	Beta poloidal	dimensionless	1	15Hz	Beta poloidal
$\kappa$	Elongation at plasma boundary	dimensionless	1	15Hz	Elongation at plasma boundary
$l_i$	Internal inductance	dimensionless	1	15Hz	Internal inductance
$q_0$	q at magnetic axis	dimensionless	1	15Hz	q at magnetic axis
$q_{95}$	q at 95% flux surface	dimensionless	1	15Hz	q at 95% flux surface
Feedback Signal					
IC1	In-vessel coil no.1 current	A	1	1kHz	In-vessel Rogowski coil no.1 current
Input Signals					
Ref. $I_p$	Reference plasma current	A	1	1kHz	Reference plasma current
PF	Current of Poloidal field (PF) coils	A	14	1kHz	PF 0-14 current
$B_{t0}$	Toroidal magnetic field	T	1	1kHz	Toroidal field at magnetic axis
LHW	Power of Lower Hybrid Wave Current Drive and Heating System	kW	4	20kHz	2.45 GHz LHW, and 4.6 GHz LHW
NBI	Neutral Beam Injection System	Raw signal	8	5kHz	Acceleration voltage and beam current, of No. 1-2 left/right ion source.
ICRH	Ion Cyclotron Resonance Heating System	Raw signal	16	5kHz	Output of detector for rejected power of No. 1-16 transmitter
ECRH/	Electron Cyclotron Resonance Heating/Current Drive System	Raw signal	4	50kHz	Output of detector for injected power measurement No. 1-4 gyrotron
GPS	Gas Puffing System	Raw signal	12	10kHz	Horizontal ports J, K, D, B; Upper port O; Lower ports O, C, H
SMBI	Supersonic Molecular Beam Injection	Raw signal	3	10kHz	3 ports of SMBI
PIS	Pellet Injection System	Raw signal	1	10kHz	1 injection line for Pellet Injection
Ref. Shape	Shape reference	Raw signal	20	1kHz	11 groups of control points

least one available model output signals. If there is not a certain magnetic field configuration, it is impossible to constrain (or control) the plasma. Furthermore, it is meaningless to model the tokamak discharge without complete actual  $I_p$ . Additionally, the deep model training or test will be impossible if all the model output signals are unavailable. Three different data sets are needed while developing the bidirectional LSTM model for discharge modeling. A training set is required for training the model. A validation set is needed to determine which hyper-parameters are best. A test set is used to measure the final accuracy of the deep learning model. The training set should use the earliest data of the selected EAST campaign to simulate the new data faced in practice. The test set and validation set are assumed to be statistically similar, so we can expect the best performance on the test set by optimizing the accuracy on the validation set. For each epoch, the model must input every shot in the validation set to get the performance metric, and the validation set is not be used to update the model parameters. So relatively small validation set can accelerate the model training. The shot range of the validation set and the test set should not cross to ensure the objectivity of the test set. The test set should only be used once at last. In other words, the test set should be used only for model testing and should not be present during the model training or tuning phase. These three data sets are made extremely carefully to meet these strict requirements. Shot #14866-74999 in the EAST database are selected as the training set. 21192 normal shots are reserved at last. The validation set has shot numbers in the range #75000-77000. Shots #77000-88283 are in the test set.

All data are resampled with the same sample rate  $1kHz$ . Although we used a relatively low sampling rate, the original resampled data set still contains 547GB data. Therefore for each shot, the data is saved to an HDF5 file, not in the database server for quick and robust training. The metadata is stored in MongoDB for double-checking the data validity and availability by the human and program.

There are significant differences in the sampling rate of raw signals  $R_{raw}$ , So the input and output signal data sets need to be resampled at a common sampling rate  $R_c$  to ensure that the data points of different signals are aligned at the same time. If  $R_{raw} < R_c$ , the raw signal data needs to be linearly interpolated to increase the sampling frequency. If  $R_{raw} > R_c$ , the raw signal data needs to be down-sampled into the same sampling rate with  $R_c$  by simple moving average (SMA). In the present work, the simple moving average (SMA) calculates the average of a specific time range ( $1/R_c$ ) of values. The SMA used the information from the later time, but our work aims to create offline modeling. Since we use bidirectional LSTM for the model, having as objective offline discharge modeling, we remove the causality constraint for the sequences fed to the model for training. From another perspective, since high-frequency fluctuations are not a relevant outcome of the experimental proposal stage, we process the data by filtering out high-frequency fluctuations.

#### 4.2. Standardizing

Firstly, all source data was saved in the HDF5 file. Then, discharge duration time and every signal mean, variance, existence flag will be saved to the MongoDB database shot-by-shot. Saving the mean and variance of each signal of each shot data is necessary not only to double-check the presence of outliers in the signals but also for calculating the global means and standard deviations for the huge data by MapReduce. If a signal in a shot has outliers, then the signal values in this shot will not be used to calculate the signal's global mean and standard deviation. MapReduce is a programming model and an associated implementation for processing and generating big data sets with a parallel, distributed algorithm on a cluster. The reasons for using MapReduce are that

large-scale data will be overflowed if the global mean and standard deviation are calculated directly. When the source data means and standard deviations have been calculated, the z-scores will be applied for standardization. In this step, if the input data have NaN (invalid value) or Inf (infinite value) will be replaced by linear interpolation value and  $3.2 \times 10^{32}$  (it is not the maximum value of the float type, but it is large enough. And it can still be calculated without overflowing) respectively). In statistics, the z-score is the number of standard deviations by which the value of a raw score (i.e., an observed value or data point) is above or below the mean value of what is being observed or measured. Raw scores above the mean have positive standard scores, while those below the mean have negative standard scores. Z-score is calculated by  $z = (x - \mu)/\sigma$  where  $\mu$  is the mean of the population.  $\sigma$  is the standard deviation of the population.

#### 4.3. Bucketing batchwise training.

Mini-batching gradient descent [46, 47] is a useful practice for improving GPU performance [48] and accelerating the training convergence of deep-learning models. The parameter loss gradients are computed for several examples in parallel and then averaged. For this to work efficiently, the architecture for the forward and backward pass of each gradient computation needs to be equal for all the examples computed in parallel. This is not possible if different training examples have different lengths. Thus, training RNN or its variants on a large amount of data with different lengths is a significant and challenging problem. Bucketing [49] was used to solve this problem in the present work.

The bucketing method can be reduced to a partition problem. Let  $S = \{s_1, s_2, \dots, s_n\}$  be the set of sequences and  $l_i = |s_i|$  is the length of sequence  $s_i$ . Each GPU processes sequences in a mini-batch in a synchronized parallel manner, so processing time of a mini-batch  $I_{\text{batch}} = \{s_1, s_2, \dots, s_k\}$  is proportional to  $O(\max_{i \in 1, \dots, k} l_i)$  and processing time of the whole set is expressed as:

$$T(S) = O(n/k * \max_{i \in 1, \dots, k} l_i) \quad (4)$$

If the dataset sequences were shuffled randomly before splitting, the minimum and maximum sequence length in the mini-batch would be very different. As a result, the GPU would do additional work for processing the meaningless tails of shorter sequences. Additionally, the too-long sequence with a non-suitable batch size will be overflowed due to the GPU memory capacity limit. Specifically, if we use the same batch size for long sequences input as for short sequences input, it will take up more GPU memory which will easily cause overflows. We used customized bucketing to optimize the batch training to overcome this flaw and decrease training time. As shown in the figure 2, we cluster all sequences to  $B$  buckets by the lengths. Let  $S_i = \{s_{j_1}, s_{j_2}, \dots, s_{j_{k_i}}\}$ . For every bucket, we perform the mini-batch training with different batch sizes. The processing time of the whole set is expressed as:

$$T(S) = \sum_{i=1}^B O(T(S_i)) \quad (5)$$

We manually partitioned the sequence length set in the present work because the different sequences length sets will use different batch sizes. The result of the partition is shown in figure 2. The Bucket 1,2,3 is in the interval [2, 12.3], (12.3, 50], (50, 412] respectively. Because of the GPU memory capacity limit, the batch size of the three buckets is set 8,4,1 respectively. These batch sizes can control GPU memory overflow and easily allocate the input tensor for each GPU.

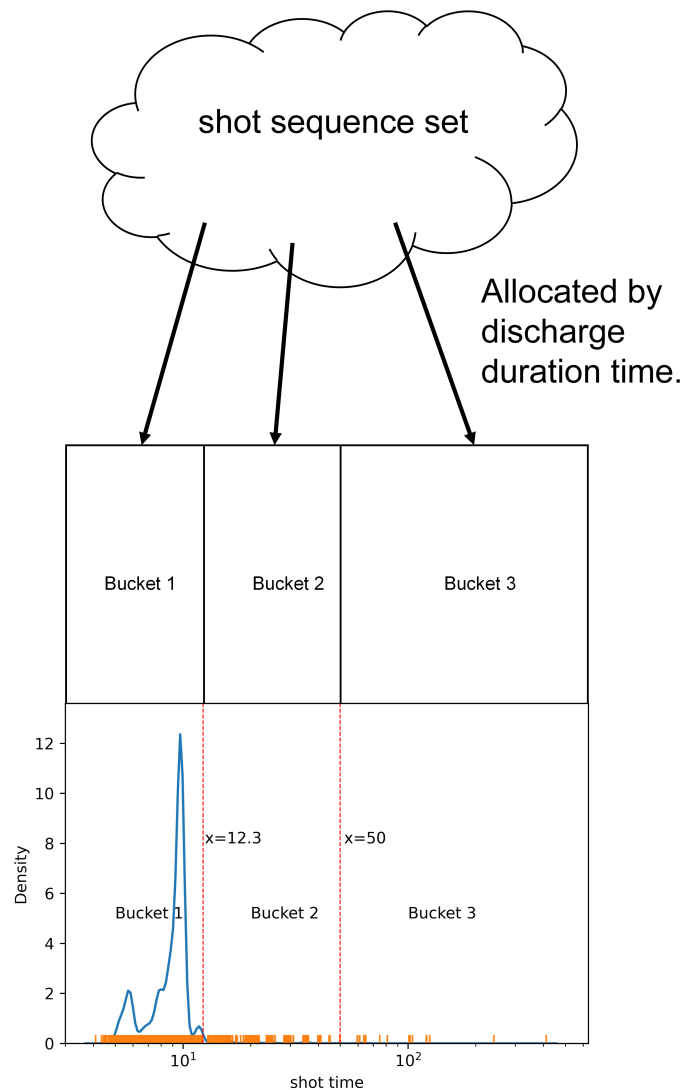


**Figure 2.** The shots during time distribution of the input discharge sequences. The number of buckets  $B = 3$ .

The sequences within every bucket were shuffled randomly. And then, the sequences were generated batch sequences batch-by-batch. To train batchwise with a batch size  $M$ , we need  $M$  independent shot discharge sequences of the same bucket to feed to the GPU. The different length discharge sequences were padded by zeros to the same length. We do this by using  $M$  processes to read sequence data in parallel. The  $M$  sequences were fed to a buffer first to solve the problem of GPU and CPU speed mismatch since data from HDF5 files are read through a CPU.

#### 4.4. Model training

IC1 is an in-vessel Rogowski coil current [45, 50], and this current does not have a direct reference signal. In theory, when controlling the tokamak magnetic field, in-vessel current is an essential feedback signal that directly impacts the magnetic field profile [45]. Moreover, In practice,  $l_i$ ,  $\beta_n$  can not be accurately estimated by the input signals that do not include IC1. Finally, the IC1 signal can not be programmable or manual setting in the experiment proposal stage. Therefore, first, we train a machine learning model (same model architect as depicted in figure 1) to reconstruct IC1. Secondly, we connected the trained IC1 reconstruction model and the diagnostic parameters reconstruction model for training, where the IC1 reconstruction part was fine-tuned using a minimal learning rate.

The model for reconstructing IC1 and the diagnostic parameters has the same architecture, in which only the input and output are different. The input of the IC1 reconstruction includes all input signals in table 1. The input of the diagnostic parameters reconstruction includes the output of the IC1 reconstruction model and does not use the shape reference signals. The training process is similar to using the trained model, as shown in figure 3.

The deep learning model uses end-to-end training executed on 8x Nvidia P100 GPUs with PyTorch [51] on the Centos7 operating system. The weight initialization scheme for the deep learning model is Xavier initialization [52], bias initializer is zeros, and optimizer is RMSprop [53]. The loss function of this training should be noted. The function is Masked MSELoss, which has some improvements for mean squared error (MSE) loss function. The MaskedMSEloss can be described as:

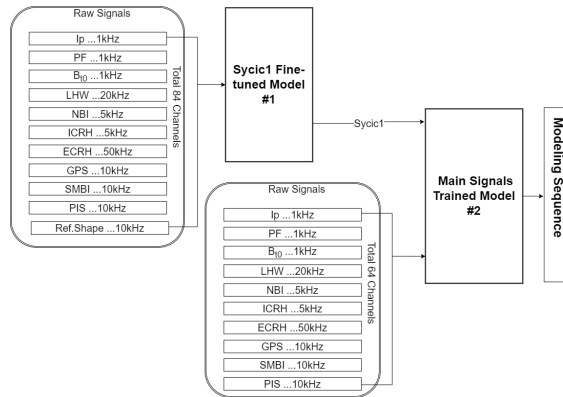
$$l(\mathbf{x}, \mathbf{y}) = L = \frac{\sum_{i=0}^{i=N} \{l_1, l_2, \dots, l_N\}}{N}, \quad (6)$$

$$l_i = \sum_{j=0}^{j=\text{len}} (\mathbf{x}_j^i - \mathbf{y}_j^i)^2, \quad (7)$$

where  $N$  is the batch size,  $\mathbf{x}$  and  $\mathbf{y}$  are the batch experimental sequence and batch predicted sequence,  $\mathbf{x}_j^i$ ,  $\mathbf{y}_j^i$  are the  $j$ th point values of the  $i$ th experimental sequence and predicted sequence. The subtlety of this work is “ $j = \text{len}$ ”, where “ $\text{len}$ ” is the length of the  $i$ th sequence. So the masked MSE function can prevent useless training of the zeros padding section of the sequence. The training of our model is executed several times. Many of these trials are considered as failed (e.g., divergence in training, poor performance on the validation set, etc) because of unsuitable hyper-parameters. In the process of training our model, multiple sets of hyperparameters were tried. It was a trial-and-error approach on different sets of hyperparameters combinations: the best hyperparameter set was chosen based on the best validation set performances. Finally, the best hyper-parameters were found and shown in table 2.

**Table 2.** Hyperparameters in this model

Hyperparameter	Explanation	Best value
$\eta$	Normal learning rate	$1 \times 10^{-3}$
$\eta_f$	fine-tuning learning rate	$1 \times 10^{-4}$
$\gamma$	Momentum factor	0.5
L2	L2 regularization rate	0.01
Loss function	Loss function type	Masked MSE
Optimizer	Optimization scheme	RMSprop
Dropout	Dropout probability	0.1
dt	Time step	1ms
Batch_size	Batch size	8,4,1
RNN_type	Type of RNN	Bidirectional LSTM
$n_{rnn}$	Number of RNN stacked	4
$H_{rnn}$	Hidden size of RNN	512
$n_{encoder}$	Number of BiLSTMs stacked in encoder	2
$n_{decoder}$	Number of BiLSTMs stacked in decoder	2

**Figure 3.** Using the trained model.

## 5. Results

After the deep learning model has been trained, the model can be tested on unseen data (test set), as shown in figure 3. In the present work, models are used in sequence. The #1 deep learning model is used first to get the IC1 estimated values and then the #2 deep learning model to estimate the tokamak's main diagnostic signals. The preprocessing steps on new data are the same as before, keeping the training set parameters (the mean  $\mu$  and the standard deviation  $\sigma$ ) for standardization. The data whose distribution lies outside of the training set, as it was scaled with the training's standardization parameters, might affect the model's generalization capabilities. The model is trained with the standardized data and produces as output the estimated values of the diagnostic signals. In the final step, the corresponding model should be selected according to the diagnostic signal to be modeled.

In this section, the modeling results will be analyzed in detail, including representative modeling

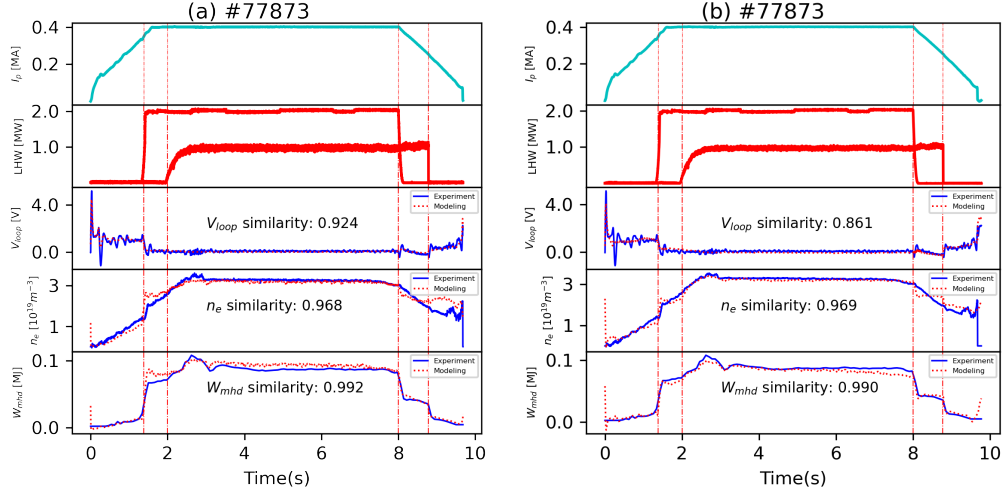


**Figure 4.** The comparison of the modeling results between the bidirectional LSTM (a) and encoder-decoder model (b) in a typical shot #77873. The vertical dash-dot lines indicate the rising and falling edges of the external auxiliary system signal and the plasma response.

results and similarity distributions. In the present work, similarity and mean square error (MSE) are used as quantitative measurements of the modeling results accuracy.

$$S(\mathbf{x}, \mathbf{y}) = \max \left( \frac{\Sigma(\mathbf{x} - \bar{\mathbf{x}})(\mathbf{y} - \bar{\mathbf{y}})}{\sqrt{\Sigma(\mathbf{x} - \bar{\mathbf{x}})^2 \Sigma(\mathbf{y} - \bar{\mathbf{y}})^2}}, 0 \right), \quad (8)$$

$$MSE(\mathbf{x}, \mathbf{y}) = \frac{1}{n} \sum_{i=1}^n (\mathbf{x}_i - \mathbf{y}_i)^2, \quad (9)$$

where  $\mathbf{x}$  is experimental data,  $\mathbf{y}$  is modeling result,  $\bar{\mathbf{x}}$ ,  $\bar{\mathbf{y}}$  are the means of the vector  $\mathbf{x}$  and vector  $\mathbf{y}$ ,  $\mathbf{x}_i$ ,  $\mathbf{y}_i$  are the point values of the vector  $\mathbf{x}$ ,  $\mathbf{y}$ . The MSE is the mean ( $\frac{1}{n} \sum_{i=1}^n$ ) of the squares of the errors  $(\mathbf{x}_i - \mathbf{y}_i)^2$ . MSE will be affected by the outlier. Similarity can only measure whether the trend is consistent, but it cannot measure the difference in value.

### 5.1. Comparison.

In the previous work, we showed the results for three output diagnostic signals (i.e.  $n_e$ ,  $W_{mhd}$ , and  $V_{loop}$ ). In order to have a reasonable comparison with the results in [1], we evaluate the model using the same training, validation and test sets of the previous work.

As shown in figure 4, a typical EAST normal discharge shot #77873 (already presented in our previous paper [1]) is selected to check the difference between previous and present work. Shot # 77873 has two LHW injections during discharge. Experimental data and modeling results are shown together in figure 4. The comparison shows the bidirectional LSTM can get better modeling results of  $V_{loop}$  than the encoder-decoder model while not using adaptive resampling.

The same test shot set (with 695 shots) as in the previous work was used to evaluate the improvement of the model quantitatively. The compared statistical results with previous work about

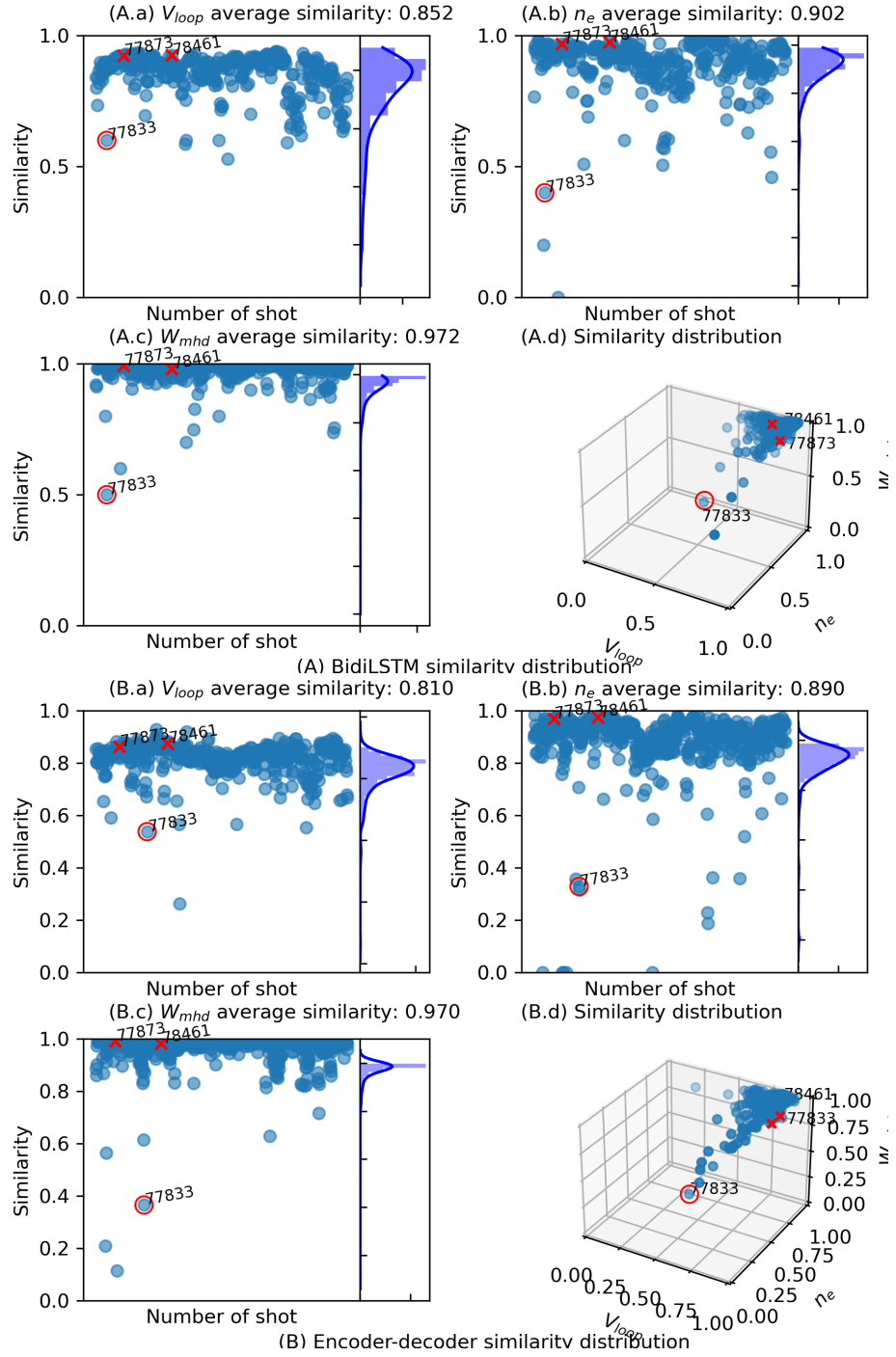


**Figure 5.** The comparison of similarity distribution of the same output signals ( $V_{loop}$ ,  $n_e$ , and  $W_{mhd}$ ) in the same test set with previous work. The marked shots are from the previous work to show consistency between the two works.

**Table 3.** The average similarity and MSE of the eleven diagnostic signals.

Output signals	Average similarity	Average MSE
Act. $I_p$	0.986	0.0015
$n_e$	0.902	0.363
$W_{mhd}$	0.972	0.077
$V_{loop}$	0.852	0.379
$\beta_n$	0.961	0.062
$\beta_t$	0.970	0.130
$\beta_p$	0.915	0.179
$\kappa$	0.961	0.0019
$l_i$	0.916	0.127
$q_0$	0.878	0.129
$q_{95}$	0.944	0.093

the similarity between model results and the experimental data are shown in figure 5. Compared with the previous work, the model used in the present work has a higher similarity on average for all the three reconstructed output signals ( $W_{mhd}$ ,  $n_e$  and  $V_{loop}$ ), which can be seen in the multivariate joint probability distribution as well. This feature shows that the bidirectional LSTM can better model the normal discharge shot. The bidirectional LSTM has similar outliers with previous work in the distribution. As depicted in figure 5, those points far away from the center of the cluster indicate that the experiment is running in abnormal mode [1]. The bidirectional LSTM has increased by  $\sim 5\%$  similarity in  $V_{loop}$  modeling results while not using the adaptive resampling. And it has not improved in  $W_{mhd}$ , the authors think the reason is  $W_{mhd}$  is good enough in the previous work. Further big improvement can not be achieved by the bidirectional LSTM. The present model improves the similarity performance of  $n_e$  by  $\sim 1\%$ . As shown in figure 4, the  $n_e$  bidirectional modeling result is more sensitive to changes of the external drives than the encoder-decoder modeling result. This feature may be the reason why the improvement of  $n_e$  similarity performance is only  $1\%$ . If the extended data was used, the  $n_e$  and  $V_{loop}$  similarity could be improved by  $\sim 1.9\%$  and  $\sim 7\%$ , respectively.

### 5.2. More key diagnostic signals.

As mentioned earlier, only three signals are still not enough for tokamak discharge modeling, and a physical model code should be involved for estimating the actual  $I_p$  of input signals. In the present work, the bidirectional LSTM can reproduce the multiple diagnostic signals, from ramp-up to ramp-down, without relying on a physical code. The model accurately reproduces the slope of the ramp-up and the amplitude of the flat-top. The model can also reflect the external auxiliary system signal impact on the diagnostic signal. As shown in figure 6, the vertical dash-dot lines indicate the rising and falling edges of the external auxiliary system signals and the plasma response. In the figure 6, we add the loss of each modeling signal for the more accurate comparison modeling and experimental signals. The MSE loss can more accurately measure the difference of values.

The whole test data set of shot range 77000-88283 is used to quantitatively evaluate the reliability of the modeling results of the other eight signals. The statistical results of the similarity and MSE between modeling results and experimental data are shown in figure 7 and in table 3.

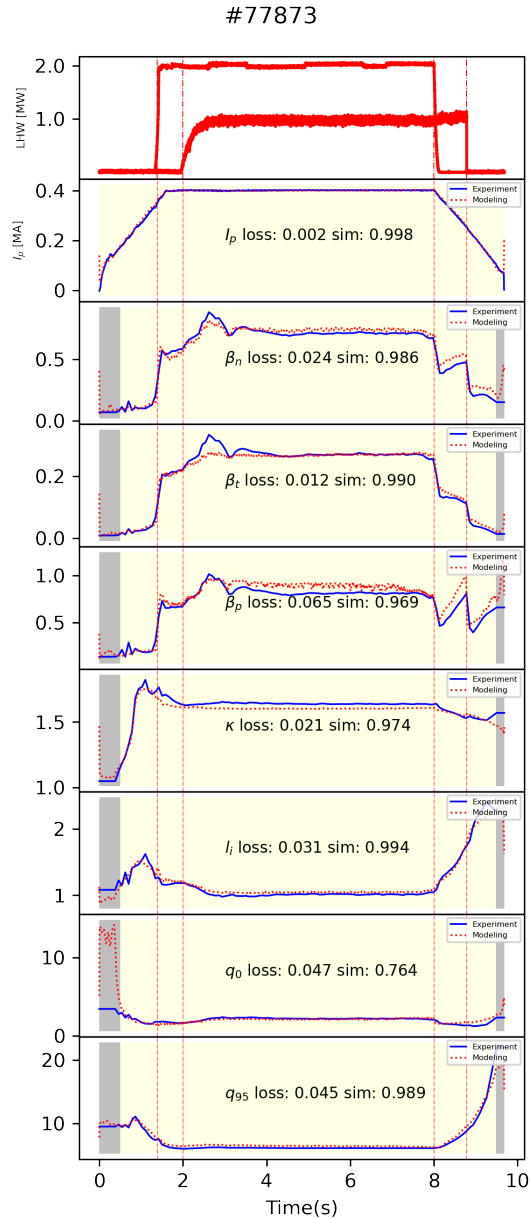


**Figure 6.** Comparison of the modeling result and EAST experiment data. No experimental data are available for the gray area, so the modeling results for this area are unreliable.

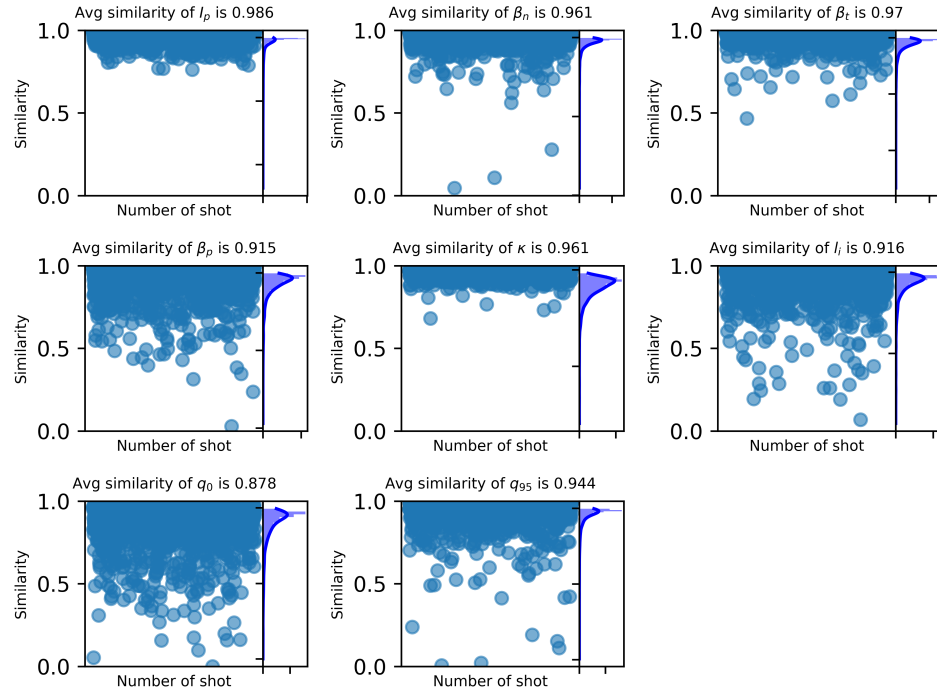


**Figure 7.** The similarity distribution and average similarity in the whole test set. The figure shows the similarity distributions of the output signals (see table 1) excluded  $W_{mhd}$ ,  $n_e$  and  $V_{loop}$ .

Except for  $q_0$ , the average similarity of other key signals is greater than 90%. And the similarity distribution is concentrated above 90%. The average similarity of  $q_0$  is greater than 85%. This quantity has a poor similarity, because if the equilibrium reconstruction is not properly constrained with pressure profiles and kinetic measurements,  $q_0$  might be unreliable. Since it might suffer of large variance, as the model is struggling mostly for the reconstruction of that parameter.

All selected key diagnostic signals excluding  $V_{loop}$  can be considered to have been almost completely modeled under the normal discharge condition. Most of the errors in the reconstruction of  $V_{loop}$  are related to the plasma start-up and shut-down phases respectively.

## 6. Conclusion and discussion

In previous work, we have introduced the potential that machine learning can assist in experimental data analysis and proposal validation. In the present work, we show the improvement of modeling the tokamak discharge process using experimental data-driven methods. The bidirectional LSTM was developed to introduce the contextual information of discharge sequence to achieve a more accurate model. The model was trained on the EAST experimental dataset in shot range #14866-88283. This model can use the actuators signals to reproduce the normal discharge evolution process (i.e. electron density  $n_e$ , store energy  $W_{mhd}$ , loop voltage  $V_{loop}$ , actual plasma current  $I_p$ ,

normalized beta  $\beta_n$ , toroidal beta  $\beta_t$ , beta poloidal  $\beta_p$ , elongation at plasma boundary  $\kappa$ , internal inductance  $l_i$ ,  $q$  at magnetic axis  $q_0$  and  $q$  at 95% flux surface  $q_{95}$ ) without having as input any physical models and the adaptive resampling points. Benefiting from without using these two tricks, the present model is more efficient than the previous one. Since the actual  $I_p$  estimation of the whole tokamak discharge process using simulation code takes much time [2, 54, 55], and adaptive resampling more points on ramp-up and ramp-down phases also consumes more time on model training and inference. Moreover, bidirectional LSTM architecture is robust to outliers. The average similarity of all the selected key diagnostic signals between modeling results and the experimental data are greater than 90%, except for the  $V_{loop}$  and  $q_0$ . These results show it is close to practical to use only the experimental data-driven model to assist in experimental data analysis and proposal validation.

The present work demonstrates that the model can easily be extended to more diagnostic signals. Compared with physical models, experimental data-driven models have a good performance on long-time scales. When the machine learning model has been trained, running a trained machine learning model is taken a shorter time than running a physic model for the whole process of tokamak discharge modeling. The present work shows a promising result using experimental data-driven modeling as a supplement to physical-driven modeling tokamak. In future work, we want to integrate the model into the plasma control system (PCS) for automatically checking control strategy. 1D and 2D plasma profiles (kinetic quantities, radiation distribution) are particularly important as well for tokamak discharge modeling, since they can support scenario development with particular reference to operational limits in high-performance scenarios [56].

### Acknowledgments

The authors would like to thank all the members of EAST Team for providing such a large quantity of past experimental data. The authors sincerely thank Qiping Yuan, Ruirui Zhang, and Jinping Qian for explaining the experimental data.

This work was supported by the National Key R&D project under Contract No.Y65GZ10593, the National MCF Energy R&D Program under Contract No.2018YFE0304100, and the Comprehensive Research Facility for Fusion Technology Program of China under Contract No. 2018-000052-73-01-001228.

### References

- [1] Chenguang Wan, Zhi Yu, Feng Wang, Xiaojuan Liu, and Jiangang Li. Experiment data-driven modeling of tokamak discharge in EAST. *Nuclear Fusion*, 61(6):066015, jun 2021.
- [2] Gloria L. Falchetto, David Coster, Rui Coelho, B. D. Scott, Lorenzo Figini, Denis Kalupin, Eric Nardon, Silvana Nowak, Luis Lemos Alves, Jean-François F. Artaud, V. Basiuk, João P.S. Bizarro, C. Boulbe, A. Dinklage, D. Farina, B. Faugeras, J. Ferreira, A. Figueiredo, Ph Huynh, F. Imbeaux, I. Ivanova-Stanik, T. Jonsson, H. J. Klingshirn, C. Konz, A. Kus, N. B. Marushchenko, G. Pereverzev, M. Owsiaik, E. Poli, Y. Peysson, R. Reimer, J. Signoret, O. Sauter, R. Stankiewicz, P. Strand, I. Voitsekhovitch, E. Westerhof, T. Zok, and W. Zwingmann. The European Integrated Tokamak Modelling (ITM) effort: Achievements and first physics results. *Nuclear Fusion*, 54(4):43018, 2014.
- [3] Paul Bonoli, Lois Curfman McInnes, C Sovinec, D Brennan, T Rognlien, P Snyder, J Candy, C Kessel, J Hittinger, and L Chacon. Report of the Workshop on Integrated Simulations for

Magnetic Fusion Energy Sciences. Technical report, Massachusetts Institute of Technology, 2015.

[4] Julian Kates-Harbeck, Alexey Svyatkovskiy, and William Tang. Predicting disruptive instabilities in controlled fusion plasmas through deep learning. *Nature*, 568(7753):526–531, apr 2019.

[5] W.H. H. Hu, Cristina Rea, Q.P. P. Yuan, K.G. G. Erickson, D.L. L. Chen, Biao Shen, Yao Huang, J.Y. Y. Xiao, J.J. J. Chen, Y.M. M. Duan, Yang Zhang, H.D. D. Zhuang, J.C. C. Xu, K.J. J. Montes, R.S. S. Granetz, Long Zeng, J.P. P. Qian, B.J. J. Xiao, and J.G. G. Li. Real-time prediction of high-density EAST disruptions using random forest. *Nuclear Fusion*, 61(6):066034, jun 2021.

[6] Bihao H Guo, Dalong L Chen, Biao Shen, Cristina Rea, Robert S Granetz, Long Zeng, Wenhui H Hu, Jinping P Qian, Youwen W Sun, and Bingjia J Xiao. Disruption prediction on EAST tokamak using a deep learning algorithm. *Plasma Physics and Controlled Fusion*, 63(11):115007, nov 2021.

[7] B. Cannas, A. Fanni, P. Sonato, and M.K. Zedda. A prediction tool for real-time application in the disruption protection system at JET. *Nuclear Fusion*, 47(11):1559–1569, nov 2007.

[8] Barbara Cannas, Rita Sabrina Delogu, ALESSANDRA Fanni, P Sonato, MARIA KATIUSCIA Zedda, and JET-EFDA Contributors. Support vector machines for disruption prediction and novelty detection at JET. *Fusion engineering and design*, 82(5-14):1124–1130, 2007.

[9] Barbara Cannas, Alessandra Fanni, G Pautasso, G Sias, and P Sonato. An adaptive real-time disruption predictor for ASDEX Upgrade. *Nuclear Fusion*, 50(7):075004, jul 2010.

[10] R Yoshino. Neural-net disruption predictor in JT-60U. *Nuclear Fusion*, 43(12):1771–1786, dec 2003.

[11] M. Honda and E. Narita. Machine-learning assisted steady-state profile predictions using global optimization techniques. *Physics of Plasmas*, 26(10), 2019.

[12] O Meneghini, S P Smith, P B Snyder, G M Staebler, J Candy, E Belli, L Lao, M Kostuk, T Luce, T Luda, J M Park, and F Poli. Self-consistent core-pedestal transport simulations with neural network accelerated models. *Nuclear Fusion*, 57(8):86034, jul 2017.

[13] O Meneghini, G Snoep, B C Lyons, J McClenaghan, C S Imai, B Grierson, S P Smith, G M Staebler, P B Snyder, J Candy, E Belli, L Lao, J M Park, J Citrin, T L Cordemiglia, A Tema, and S Mordijk. Neural-network accelerated coupled core-pedestal simulations with self-consistent transport of impurities and compatible with {ITER} {IMAS}. *Nuclear Fusion*, 61(2):26006, dec 2020.

[14] Diogo R Ferreira, Pedro J Carvalho, and J E T Contributors. Deep Learning for Plasma Tomography in Nuclear Fusion. pages 1–5, 2020.

[15] O Barana, A Murari, P Franz, L C Ingesson, and G Manduchi. Neural networks for real time determination of radiated power in JET. *Review of scientific instruments*, 73(5):2038–2043, 2002.

[16] A Murari, P Arena, A Buscarino, L Fortuna, and M Iachello. On the identification of instabilities with neural networks on JET. *Nuclear Instruments and Methods in Physics Research Section A: Accelerators, Spectrometers, Detectors and Associated Equipment*, 720:2–6, 2013.

- [17] M D Boyer, S Kaye, and K Erickson. Real-time capable modeling of neutral beam injection on {NSTX}-U using neural networks. *Nuclear Fusion*, 59(5):56008, mar 2019.
- [18] A Murari, D Mazon, N Martin, G Vagliasi, and M Gelfusa. Exploratory Data Analysis Techniques to Determine the Dimensionality of Complex Nonlinear Phenomena: The L-to-H Transition at JET as a Case Study. *IEEE Transactions on Plasma Science*, 40(5):1386–1394, may 2012.
- [19] A Murari, J Vega, D Mazon, D Patané, G Vagliasi, P Arena, N Martin, N F Martin, G Rattá, and V Caloone. Machine learning for the identification of scaling laws and dynamical systems directly from data in fusion. *Nuclear Instruments and Methods in Physics Research Section A: Accelerators, Spectrometers, Detectors and Associated Equipment*, 623(2):850–854, 2010.
- [20] P Gaudio, A Murari, M Gelfusa, I Lupelli, and J Vega. An alternative approach to the determination of scaling law expressions for the L{‐}H transition in Tokamaks utilizing classification tools instead of regression. *Plasma Physics and Controlled Fusion*, 56(11):114002, oct 2014.
- [21] B Cannas, S Carcangiu, A Fanni, T Farley, F Militello, A Montisci, F Pisano, G Sias, and N Walkden. Towards an automatic filament detector with a Faster R-CNN on MAST-U. *Fusion Engineering and Design*, 146:374–377, 2019.
- [22] D. J. Clayton, K. Tritz, D. Stutman, R. E. Bell, A. Diallo, B P LeBlanc, and M. Podestà. Electron temperature profile reconstructions from multi-energy SXR measurements using neural networks. *Plasma Physics and Controlled Fusion*, 55(9):095015, sep 2013.
- [23] Daniel Böckenhoff, Marko Blatzheim, Hauke Hölbe, Holger Niemann, Fabio Pisano, Roger Labahn, and Thomas Sunn Pedersen. Reconstruction of magnetic configurations in W7-X using artificial neural networks. *Nuclear Fusion*, 58(5):56009, mar 2018.
- [24] E Coccorese, C Morabito, and Raffaele Martone. Identification of noncircular plasma equilibria using a neural network approach. *Nuclear Fusion*, 34(10):1349, 1994.
- [25] Chris M Bishop, Paul S Haynes, Mike E U Smith, Tom N Todd, and David L Trotman. Fast feedback control of a high temperature fusion plasma. *Neural Computing & Applications*, 2(3):148–159, 1994.
- [26] Young-Mu Jeon, Yong-Su Na, Myung-Rak Kim, and Y S Hwang. Newly developed double neural network concept for reliable fast plasma position control. *Review of Scientific Instruments*, 72(1):513–516, 2001.
- [27] S. Y. Wang, Z. Y. Chen, D. W. Huang, R. H. Tong, W. Yan, Y. N. Wei, T. K. Ma, M. Zhang, G. Zhuang, Huang D W Tong R H Yan W Wei Y N Ma T K Zhang M Wang S Y Chen Z Y, Zhuang G, S. Y. Wang, Z. Y. Chen, D. W. Huang, R. H. Tong, W. Yan, Y. N. Wei, T. K. Ma, M. Zhang, and G. Zhuang. Prediction of density limit disruptions on the j-TEXT tokamak. *Plasma Physics and Controlled Fusion*, 58(5), apr 2016.
- [28] Semin Joung, Jaewook Kim, Sehyun Kwak, J. G. Bak, S. G. Lee, H. S. Han, H. S. Kim, Geunho Lee, Daeho Kwon, and Y.-C. C. Ghim. Deep neural network Grad-Shafranov solver constrained with measured magnetic signals. *Nuclear Fusion*, 60(1):16034, dec 2020.
- [29] B Ph. van Milligen, V Tribaldos, and J A Jiménez. Neural Network Differential Equation and Plasma Equilibrium Solver. *Phys. Rev. Lett.*, 75(20):3594–3597, nov 1995.

- [30] Chris M Bishop, Paul S Haynes, Mike E U Smith, Tom N Todd, and David L Trotman. Real-time control of a tokamak plasma using neural networks. *Neural Computation*, 7(1):206–217, 1995.
- [31] Bin Yang, Zhenxing Liu, Xianmin Song, and Xiangwen Li. Design of {HL}-2A plasma position predictive model based on deep learning. *Plasma Physics and Controlled Fusion*, 62(12):125022, nov 2020.
- [32] T Wakatsuki, T Suzuki, N Hayashi, N Oyama, and S Ide. Safety factor profile control with reduced central solenoid flux consumption during plasma current ramp-up phase using a reinforcement learning technique. *Nuclear Fusion*, 59(6), may 2019.
- [33] H. Rasouli, C. Rasouli, and A. Koohi. Identification and control of plasma vertical position using neural network in Damavand tokamak. *Review of Scientific Instruments*, 84(2), 2013.
- [34] Bin Yang, Zhenxing Liu, Xianmin Song, Xiangwen Li, and Yan Li. Modeling of the HL-2A plasma vertical displacement control system based on deep learning and its controller design. *Plasma Physics and Controlled Fusion*, 62(7):75004, jul 2020.
- [35] Jaemin Seo, Y.-S. Na, B. Kim, C.Y. Lee, M.S. Park, S.J. Park, and Y.H. Lee. Feedforward beta control in the KSTAR tokamak by deep reinforcement learning. *Nuclear Fusion*, 61(10):106010, oct 2021.
- [36] Abhilash Mathews, Manaure Francisquez, Jerry Hughes, David Hatch, Ben Zhu, and Barrett Rogers. Uncovering turbulent plasma dynamics via deep learning from partial observations. sep 2020.
- [37] Baonian Wan, Jiangang Li, Houyang Guo, Yunfeng Liang, Guosheng Xu, Liang Wang, and Xianzu Gong. Advances in H-mode physics for long-pulse operation on {EAST}. *Nuclear Fusion*, 55(10):104015, jul 2015.
- [38] Baonian Wan, Jiangang Li, Houyang Guo, Yunfeng Liang, Guosheng Xu, and Xianzhu Gong. Progress of long pulse and H-mode experiments in EAST. *Nuclear Fusion*, 53(10), 2013.
- [39] Jiangang Li, Baonian Wan, EAST Team, and Int Collaborators. Recent progress in RF heating and long-pulse experiments on EAST. *Nuclear Fusion*, 51(9, SI), sep 2011.
- [40] Trias Thireou and Martin Reczko. Bidirectional long short-term memory networks for predicting the subcellular localization of eukaryotic proteins. *IEEE/ACM Transactions on Computational Biology and Bioinformatics*, 4(3):441–446, 2007.
- [41] Mike Schuster and K.K. Paliwal. Bidirectional recurrent neural networks. *IEEE Transactions on Signal Processing*, 45(11):2673–2681, 1997.
- [42] Alex Graves and Jürgen Schmidhuber. Framewise phoneme classification with bidirectional LSTM and other neural network architectures. *Neural Networks*, 18(5-6):602–610, 2005.
- [43] Nitish Srivastava, Geoffrey Hinton, Alex Krizhevsky, Ilya Sutskever, and Ruslan Salakhutdinov. Dropout: A simple way to prevent neural networks from overfitting. *Journal of Machine Learning Research*, 15(1):1929–1958, 2014.
- [44] Feng Wang, Yueling Wang, Ying Chen, Shi Li, and Fei Yang. Study of web-based management for EAST MDSplus data system. *Fusion Engineering and Design*, 129(June 2017):88–93, apr 2018.
- [45] Gianmaria De Tommasi. Plasma Magnetic Control in Tokamak Devices. *Journal of Fusion Energy*, 38(3-4):406–436, aug 2019.

- [46] Jeffrey Dean, Greg S Corrado, Rajat Monga, Kai Chen, Matthieu Devin, Quoc V Le, Mark Z Mao, Marc'Aurelio Marc'aurelio Ranzato, Andrew Senior, Paul Tucker, Others, and Ke Yang. Large scale distributed deep networks. *Advances in neural information processing systems*, pages 1223–1231, 2012.
- [47] Zhiheng Huang, Geoffrey Zweig, Michael Levit, Benoit Dumoulin, Barlas Oguz, and Shawn Chang. Accelerating recurrent neural network training via two stage classes and parallelization. In *2013 IEEE Workshop on Automatic Speech Recognition and Understanding*, pages 326–331. IEEE, dec 2013.
- [48] Sharan Chetlur, Cliff Woolley, Philippe Vandermersch, Jonathan Cohen, John Tran, Bryan Catanzaro, and Evan Shelhamer. cuDNN: Efficient Primitives for Deep Learning. oct 2014.
- [49] Viacheslav Khomenko, Oleg Shyshkov, Olga Radyvonenko, and Kostiantyn Bokhan. Accelerating recurrent neural network training using sequence bucketing and multi-GPU data parallelization. In *2016 IEEE First International Conference on Data Stream Mining & Processing (DSMP)*, pages 100–103. IEEE, aug 2016.
- [50] B. J. Xiao, D. A. Humphreys, M. L. Walker, A. Hyatt, J. A. Leuer, D. Mueller, B. G. Penaflor, D. A. Pigrowski, R. D. Johnson, A. Welander, Q. P. Yuan, H. Z. Wang, J. R. Luo, Z. P. Luo, C. Y. Liu, L. Z. Liu, and K. Zhang. EAST plasma control system. *Fusion Engineering and Design*, 83(2-3):181–187, 2008.
- [51] Adam Paszke, Sam Gross, Francisco Massa, Adam Lerer, James Bradbury, Gregory Chanan, Trevor Killeen, Zeming Lin, Natalia Gimelshein, Luca Antiga, Alban Desmaison, Andreas Kopf, Edward Yang, Zachary DeVito, Martin Raison, Alykhan Tejani, Sasank Chilamkurthy, Benoit Steiner, Lu Fang, Junjie Bai, and Soumith Chintala. PyTorch: An Imperative Style, High-Performance Deep Learning Library. In H Wallach, H Larochelle, A Beygelzimer, F d\textquotesingle Alché-Buc, E Fox, and R Garnett, editors, *Advances in Neural Information Processing Systems 32*, pages 8024–8035. Curran Associates, Inc., 2019.
- [52] Xavier Glorot and Yoshua Bengio. Understanding the difficulty of training deep feedforward neural networks. In *Journal of Machine Learning Research*, volume 9, pages 249–256, 2010.
- [53] Alex Graves. Generating Sequences With Recurrent Neural Networks. aug 2013.
- [54] C E Kessel, R E Bell, M G Bell, D A Gates, S M Kaye, B P LeBlanc, J E Menard, C K Phillips, E J Synakowski, G Taylor, R Wilson, R W Harvey, T K Mau, P M Ryan, and S A Sabbagh. Long pulse high performance plasma scenario development for the {National} {Spherical} {Torus} {Experiment}. *Physics of Plasmas*, 13(5), 2006.
- [55] O. Meneghini, S. P. Smith, L. L. Lao, O. Izacard, Q. Ren, J. M. Park, J. Candy, Z. Wang, C. J. Luna, V. A. Izzo, B. A. Grierson, P. B. Snyder, C. Holland, J. Penna, G. Lu, P. Raum, A. McCubbin, D. M. Orlov, E. A. Belli, N. M. Ferraro, R. Prater, T. H. Osborne, A. D. Turnbull, and G. M. Staebler. Integrated modeling applications for tokamak experiments with OMFIT. *Nuclear Fusion*, 55(8):83008, 2015.
- [56] A. Pau, A. Fanni, S. Carcangiu, B. Cannas, G. Sias, A. Murari, F. Rimini, Human Immunodeficiency Virus, Associated Neurocognitive Disorders, Consensus Report, Mind Corresponding Author, and Alternate Corresponding Author. A machine learning approach based on generative topographic mapping for disruption prevention and avoidance at JET. *Nuclear Fusion*, 59(10):106017, oct 2019.